Applied Aerodynamics Conference 2014: Advanced Aero Concepts, Design and Operations,
22-24 July 2014, Bristol, UK, pp. 384-402. ISBN:9781510802698, Royal Aeronautical Society (RAeS)

Dynamic distortion simulations for curved aeronautical intakes

Chiereghin, N., MacManus, D., Savill, M., Dupuis, R.

Cranfield University, Bedford, Bedfordshire, MK430AL

Keywords: Convoluted intakes, CFD, Detached Eddy Simulation, flow distortion, S-duct, Proper Orthogonal Decomposition

Abstract

This research focuses on the numerical simulation of the dynamic distortion in highly convoluted aeronautic intakes and extends the current knowledge with a systematic study of the influence of duct diameter, Mach number and offset. A comparison against experimental data revealed the capability of Delayed Detached Eddy Simulation to reproduce the trends of variation of distortion descriptors and pressure recovery although the absolute values are not yet captured. Analysis of the temporal distribution of the flow parameters identified the relevant fluctuating components both for total pressure distortion and swirl. A Proper Orthogonal Decomposition of the flow highlighted important differences of the major flow structures for different duct curvatures and a strong dependence of the distortion parameters also on the finer flow structures.

Nomenclature

List of symbols

p	Static pressure
p_o	Total pressure
max	Maximum value of a temporal distribution
min	Minimum value of a temporal distribution
s	S-duct curvilinear coordinate along the axis
t_c	Convective time = Ls/w_i [s]
t*	a-dimensional time = t/tc
u, v, w	Velocity vector components
x, y, z	System of reference coordinates
D	Diameter
Ma	Mach number
R	S-duct curvature radius [m]
Re	Diameter-based Reynolds number
α	Swirl angle [deg]
Δt	Unsteady simulation time step [s]
Δt^*	a-dimensional time step = $\Delta t/tc$
Θ	Angular position on the AIP
Φ	S-duct angular position

Abbreviations

AIP	Aerodynamic Interface Plane
CDI	Circumferential Distortion Index
CFD	Computation Fluid Dynamics
DC(θ)	Distortion coefficient
DDES	Delayed Detached Eddy Simulation
DES	Detached Eddy Simulation
LES	Large Eddy Simulation
RANS	Reynolds Averaged Navier Stokes

RDI	Radial Distortion Index
SC(θ)	Swirl coefficient
SAE	Society of Automotive Engineering

Subscripts

AIP	Aerodynamic interface plane
Avg	Area-average
in	Inlet condition
Θ	Tangential direction

Operators

$\langle\cdot\rangle$	Time-average
$\sigma_{\cdot}$	Standard deviation

1. Introduction

Future aircraft engine configurations are expected to require a closer coupling between the propulsion system and the airframe, with relevant benefits in term of drag, noise and observability reduction. For many embedded engine systems, the complexity of the flow field associated with convoluted intakes presents an area of notable research challenges. To enable the development of novel aircraft configurations, a better understanding is required of flow distortion, non-uniform cross-sectional distribution of flow parameters and vortical structures associated with curved and complex aero-engine intakes.

In a previous experiment by Wellborn et al [1], the flow through a diffusing S-duct, with an area ratio of 1.52, was investigated. Streakline flow visualisation on the duct surface showed a separation bubble on the lower part of the wall containing two vortical structures which can be described as a result of the interaction between the boundary layer and the adverse pressure created by centrifugal acceleration of the flow in the first part of the duct. Cross-flow plane measurements, using a five-hole probe, showed that the time-averaged flow field comprised a pair of streamwise vortices at the outlet of the S-duct associated with a low pressure zone on the lower part of the plane. Such a simultaneous presence of total pressure and swirl at the inlet of the compressor has previously been demonstrated to be source of loss in surge margin, stall and vibration [2] [3]. High bandwidth pressure measurements in two similar geometries [4] [5] outlined notable instability in the separation zone which produces oscillations of the flow distortions at the exit plane, which is an additional source of loss in performance and operability for the compression system.

The recent improvement in computational resources and computational fluid dynamics (CFD) presents an opportunity to calculate flow distortion in such complex intake geometries. A comparison between different turbulence models for RANS simulations was performed previously by Delot et al [6]. Although the models could not accurately predict simultaneously all the performance parameters such as pressure recovery and total pressure distortion, it demonstrated the capability of k-ω SST to correctly broadly represent the flow physics.

An additional aspect with modern CFD methods is offered by transient simulations, which can improve the performance of Reynolds Averaged Navier-Stokes methods and provide the possibility to simulate the time-variant issues of unsteady flow distortion. Direct resolution of the flow equations is not possible with the current computational resources for the majority of the engineering application for the large range of scales to be resolved. Large Eddy Simulation (LES) are designed to resolve larger turbulent scales, more dependent on boundary conditions (BC), and model the more “universal” small scales by means of so-called subscale models. For the flow studied in this research, a hybrid version of LES, called Detached Eddy Simulation (DES), has been applied. In this approach the flow close to the surface is modelled and the in other regions the structures are resolved. A recent comparison between different DES approaches was performed by Berends et al [7] for an S-duct and Delot et al [8] for a serpentine duct typical of military unmanned aerial vehicles. A notable improvement in the flow field calculations was observed in comparison with a RANS method and previous applications together with a good capability to reproduce turbulent flow structures in separation zones, although the accuracy in prediction of pressure recovery and distortion descriptors should be further improved for more reliable industrial applications.

This current research extends the recent effort in flow distortion simulation with a parametric study of the effect of Reynolds number, Mach number and geometric offset of the S-duct. The capability of DES to predict the change in performance for different configuration is assessed with a comparison with experimental data [1] [4] [5]. In this work

dynamic behaviour of the swirl type flow features is also analysed. For a better understanding of the dynamic distortion issues, a Proper Orthogonal Decomposition of the total pressure variation at the S-duct exit plane is performed.

2. S-duct configurations and flow conditions

In this research, the S-ducts and flow conditions previously experimentally investigated by NASA and ONERA [1] [6] [5] were considered. A schematic representation is provided in Figure 1**.** In the computational models two straight duct sections have been added upstream and downstream of the S-duct to prevent any influence of the S-Duct flow field calculation from the boundary conditions. This geometry is representative of the test rig described in Wellborn et al [1]. The centerline is composed of two opposite circular arcs of extension $\phi_{max}/2$ as defined in Figure 1. The aerodynamic interface plane (AIP) is representative of the inlet conditions of a gas turbine's compression system. An area ratio of 1.52 was fixed for all the configurations (Table 1**)**.

In this work, three different configurations were considered with parameters defined in Table 1**.** S-Duct 1 has the same dimensions of the geometry experimentally investigated by Wellborn et al [1]. S-Duct 2 maintains the same non-dimensional offset H_0/L and length L/D_{in} as in S-Duct 1 but with a reduced inlet diameter. A similar geometry was experimentally investigated in [4] with only a slightly different non-dimensional length L/D_{in} of 5.2 instead of 5.0. S-Duct 3 is obtained from S-Duct 2 with an increase of the a-dimensional offset of about 1.8.

These configurations were used to perform four different simulations with nominal flow conditions outlined in Table 1. The case S-Duct 1 reproduces the condition of the Wellborn et al [1] experiment. The comparison between S-Duct 1 and S-Duct 2A provides an assessment of the effect of the scaling on the S-Duct performance. An assessment of the Mach number effect can be obtained from S-Duct 2A and 2B, and the results was compared with the data reported in Delot et al [4] [6]. Finally, the assessment of the offset effect is obtained from the comparison between S-Duct 2A and 3. The Reynolds number is based on the inlet diameter. The convective time t_c is defined as the time necessary for a particle to flow throughout the S-Duct with a constant velocity equal to the inlet one.

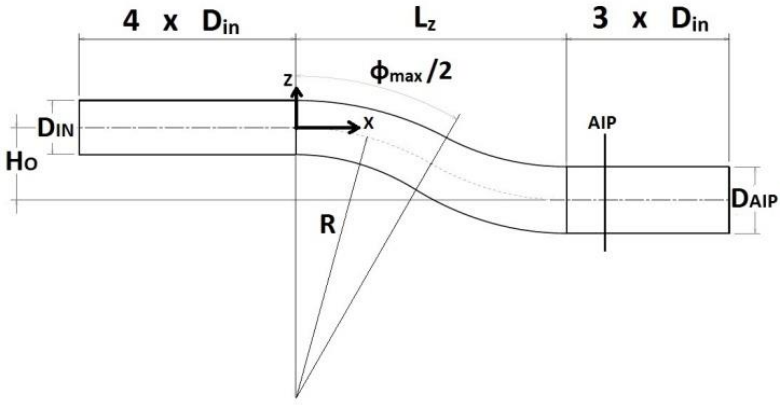

Figure 1: Geometry sketch and definition of the parameters

Parameters	S-Duct 1	S-Duct 2	S-Duct 3
A_{out}/A_{in}	1.52	1.52	1.52
L/D_{in}	5.0	5.0	4.95
Ho/L	0.268	0.268	0.493
Φ_{max} [°]	60	60	105.1
D_{in} [m]	0.2042	0.133	0.133
D_{out} [m]	0.2514	0.164	0.164
R [m]	1.021	0.665	0.4146
L [m]	1.021	0.665	0.658
Ho [m]	0.2736	0.1784	0.3245

Table 1: S-duct geometry parameters

Case	AIP Ma	Inlet Re $Re_{Din} = \frac{(\rho u D)_{in}}{\mu}$	Mass Flow [kg/s]	PO_{in}	t_c [10^{-3} s]
S-duct 1	0.36	2.6×10^6	6.2	107670	5.4
S-duct 2A	0.36	1.7×10^6	2.4	88744	3.5
S-duct 2B	0.18	1.1×10^6	1.3	88744	5.2
S-duct 3	0.39	1.8×10^6	2.6	90000	3.5

Table 2: Test cases and flow conditions: AIP Mach number, inlet diameter-based Reynolds number, mass flow, inlet total pressure and convective time.

3. Methodology

3.1.CFD method

In order to reduce the computational cost of the Navier-Stokes equations for turbulent flow, an averaging operator is applied to separate to averaged component of the flow parameter from the fluctuating part. The so called Reynolds-stress tensor defined from the correlation of the three fluctuating components of the velocity, and its elements are treated as new unknown variables and calculated from properly defined models. Many different empirical and theoretical models have been proposed to date [9], but none can be considered universally representative of all the possible fields found in practical applications. One of the most popular in aeronautics is the k-ω shear stress turbulence model (SST) which is designed for calculation of the flow with strong adverse pressure and pressure-induced separation [10], which are the main features of the flow considered in this research.

Large Eddy Simulation (LES) represents a more accurate approach to complex turbulent flows, which divides the turbulence into large scales, which are resolved directly, and small scales, which are modeled, by means of spatial filterers. Since the smaller scales are less dependent on the boundary condition, universal models can be defined. However, this methods require grid dimension to high for the resolution of near-wall turbulence structures in high Reynolds number flows (>10^6), so hybrid RANS-LES methods are commonly adopted.

In this research, the so-called Detached-Eddy-Simulation (DES) is chosen, where the flow field is calculated with RANS equations close to the wall and low-turbulent part, whilst the high-turbulent zones, in particular after the separation, are calculated with LES. The most recent "Delayed" version of the DES (DDES) is used to prevent grid-induced separation problems typical to the previous version DES 98 [11]. In this work the k-ω SST turbulence model was chosen for the closure of the RANS equations. The pressure-based solver was selected with a segregated PISO scheme for faster computations. A comparison with density-based results for the S-Duct 1 case did not showed noticeable differences. A second-order spatial interpolation scheme was used for the pressure equations and the MUSCL scheme for the others, together with a bounded-second order temporal discretization. Unsteady DDES simulations were initialized with converged steady RANS simulations with residuals lower than 10^{-8}. A time step Δt of 6 10^{-6} s was chosen for the high Mach number cases (S-Duct 1-2A-3) and 1.2 10^{-5} for the low Mach case (S-Duct 2B) which correspond to an non-dimensional time step Δt of about 0.002 with respect to the convective time.

A structured mesh with a size of 5.9 million of nodes was created with a multi-blocking strategy. In order to maintain the mesh perpendicular to the wall for every configuration, four different blocks were created: the first associated with the inlet straight duct, the second and the third with the S-Duct, and the forth with the straight duct downstream the S-Duct. The robustness of the method and the simplicity of the geometry allowed a good quality of the mesh for every case, with a 2x2x2 determinant greater than 0.8. The mesh has an H-grid structure in the central part of the duct, and an O-grid structure around the wall.

The DDES calculations were initialized with well converged RANS simulations of 10,000 iterations and residuals of an order of magnitude of 10^{-7}. Moreover, the RANS simulations provide a good agreement with the measured inlet boundary layer thickness (2.1% relative difference) but some discrepancies with the inlet displacement thickness and the momentum thickness with respectively a relative error of 9.6% and 17.9%. Twenty sub-iterations per time step and overall calculation duration of 40 convective times have been performed, where the first 10 were used as a transition between RANS steady solution and DDES unsteady flow, and the next 30 were used for statistical and spectral analysis together with POD. As regards the convergence of the unsteady simulations, the residuals show a reduction of 3 or

more order of magnitude for momentum equations at each time step. In addition, in order to check the statistically convergence with 30 throughout passages, a simulation with 15 more convective times have been performed with the S-duct 2A and the statistics of the key flow parameters (pressure recovery and flow distortion descriptors) have shown a difference of 1%.

A grid sensitivity study has been carried out for the S-duct 1 and three RANS calculations have been performed with a coarse mesh (3.1 million nodes), a medium mesh (5.9 million nodes) and a fine mesh (11.2 million nodes). The relative error for the DC(60) value is estimated to be 0.76% for the medium mesh and thus it is used for all the simulations [12]. The estimation of the DC(60) is based on the Richardson's extrapolation method [13].

The wall streak-lines of the S-duct 1 for the k-ω SST are shown in Figure 2, left. The calculations show a centreline separation point located at s_{SP}/D_{in}=2.03 and a centreline reattachment point at s_{RP}/D_{in}=4.05 which is in good agreement with the experimental data with a separation point at $s_{SP}/d1$=2.02 and a reattachment point at $s_{RP}/d1$=4.13. Furthermore, the calculation for the S-duct 2A provides a larger separation bubble with a separation point located at $s_{SP}/d1$=1.98 and a reattachment point at $s_{RP}/d1$=4.25. The decrease of the Mach number from 0.4 to 0.2 for the S-duct 2B shows a separation bubble moved slightly downstream, with $s_{SP}/d1$=1.98 for S-Duct 2A against $s_{SP}/d1$=2.04 for S-Duct 2B. However, the calculation for the S-duct 3 with the higher offset demonstrates that the bubble is smaller and translated upstream with an initial centreline separation point located at $s_{SP}/d1$=1.60 and a reattachment point at $s_{RP}/d1$=3.08.

Figure 2, center, presents the distribution of the swirl angle at the AIP, where the effect of two twin vortexes can be noticed on the lower part of the plane as an anti-symmetric distribution of α. The magnitude close to the wall is higher as an effect of the iteration of the vortexes with the wall friction. The twin vortexes originate from the separation bubble of Figure 2, left, and are also experimentally observed in Wellborn et al [1] with five-hole probe three-component velocity measurements. The distribution of pressure recovery at the AIP is presented in Figure 2, right, where is evident the effect of the flow separation on the lower part of the plane as a low total pressure zone. A similar distribution was measured in the same experiment [1], although some difference in the extension and magnitude of the low-total pressure zone is noticed, for instance, with a minimum value 5% of the inlet dynamic pressure lower than experiment in the RANS simulation.

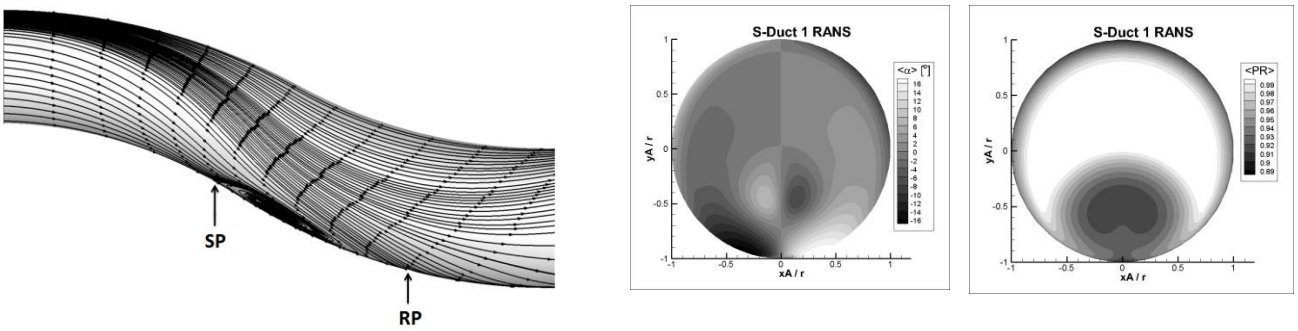

Figure 2: RANS wall streak-line visualization for S-Duct 1 case (left). Swirl angle distribution (center) and total pressure distribution (right) on the AIP.

3.2.Distortion metrics

Total pressure distortion at the AIP can be quantified by the three following descriptors: distortion coefficient DC, circumferential distortion index CDI and radial distortion index RDI. DC(60) is given by the difference between the average total pressure and the lowest average total pressure in a sector of 60° angle [14] and non-dimensionalized by the mean dynamic head q of the whole AIP

$$\mathrm{DC}(60) = \frac{\mathrm{p_{o\ avg}} - \mathrm{p_{0\ 60°\ avg}}}{\mathrm{q}} \tag{1.1}$$

where $\mathrm{p_{o\ avg}}$ is the mean total pressure and $\mathrm{p_{60°\ avg}}$ is the mean total pressure measure in a sector of 60 degrees.

The circumferential distortion index (CDI) assesses the uniformity of the circumferential total pressure distribution and is defined as [15]:

$$\mathrm{CDI} = \mathrm{Max}_{\mathrm{i=1}}^{\mathrm{n_{radius}}-1}\left(0.5\left[\frac{\mathrm{p_{0\ i}} - \mathrm{p_{0\ min_i}}}{\mathrm{p_{0,avg}}} + \frac{\mathrm{p_{0\ i+1}} - \mathrm{p_{0\ min_{i+1}}}}{\mathrm{p_{0,avg}}}\right]\right) \quad (1.2)$$

where $\mathrm{p_{0avg}}$ is the average total pressure, $\mathrm{p_{0i}}$ the average total pressure of the pressure distribution of the i-th ring and $\mathrm{p_{min_i}}$ the minimal pressure of the i-th ring.

Finally the radial distortion can be assessed by the radial distortion index (RDI). The formula follows the same logic as CDI and is defined as follows [16]:

$$\mathrm{RDI} = \mathrm{Max}\left(\frac{p_{0,avg} - \mathrm{p_{0inner\ ring}}}{p_{0,avg}}, \frac{p_{0,avg} - \mathrm{p_{0outer\ ring}}}{p_{0,avg}}\right) \quad (1.3)$$

with $\mathrm{p_{inner\ ring}}$ the average total pressure of the pressure distribution of the inner ring and $\mathrm{p_{0outer\ ring}}$ the average total pressure at the outer ring.

For the assessment of swirl distortion, two parameters are used: the SC(60) descriptor and the swirl angle. The first one has been proposed in order to quantify the swirl distortion and simply follows an analogous form to the DC(60). It corresponds to the maximum circumferential velocity in a section of 60° and is non-dimensionalized by the mean axial velocity [17]:

$$\mathrm{SC}(60) = \frac{\mathrm{Max}(\mathrm{V_\theta}(60))}{\mathrm{U_{avg}}} \quad (1.4)$$

where $\mathrm{V_\theta}(60)$ is the circumferential velocity in a 60° section and $\mathrm{U_{avg}}$ the mean axial velocity at the AIP. The swirl angle α is defined by the circumferential angle between the velocity vector and the axial velocity vector as in [2].

4. Results

4.1. Lower wall static pressure distribution

The distribution of the static pressure on the lower wall of the S-Ducts is shown in Figure 3 with numerical data compared with experimental data. Whilst a good agreement with experimental data is noticed for the low offset case Ho/L=0.2736 (S-Duct 1-2A), some difference is observed for the Ho/L=0.493 (S-Duct 3), where the re-attachment point is predicted slightly downstream in comparison with RANS and experiment (s_{RP}/L=0.57 against s_{RP}/L=0.54). However, the general trend is captured in all of the cases, where the left part of the graph shows a drop of the static pressure generated by the curvature, followed by an increase caused by the divergent shape of the ducts. The plateau in the central part represents the separation. After the separation the pressure starts rising again. For the high Mach cases, modest differences are observed for different diameter-based Reynolds numbers (S-Duct 1-2A). The offset, however, determine a remarkable drop in the pressure (S-Duct 2A against S-Duct 3). The pressure at the plateau is overestimated by CFD. Nevertheless, the trend for different configuration is well predicted also for the static pressure distribution.

The distribution of the standard deviation of the static pressure σ_p is outlined in Figure 3, normalized with the inlet dynamic pressure $p0_{in}$-p_{in}. For all of the cases the peak value is observed around the re-attachment point, which is a typical feature of separated flow and was also observed by Garnier et al [5] for the same geometry as the S-Duct 3 case. It can be inferred that a high level of turbulence is generated at the end of the separation bubble and transported by the main stream to the AIP, where, together with a distortion of the time-averaged distribution, notable fluctuations of total pressure and swirl angle distribution are observed.

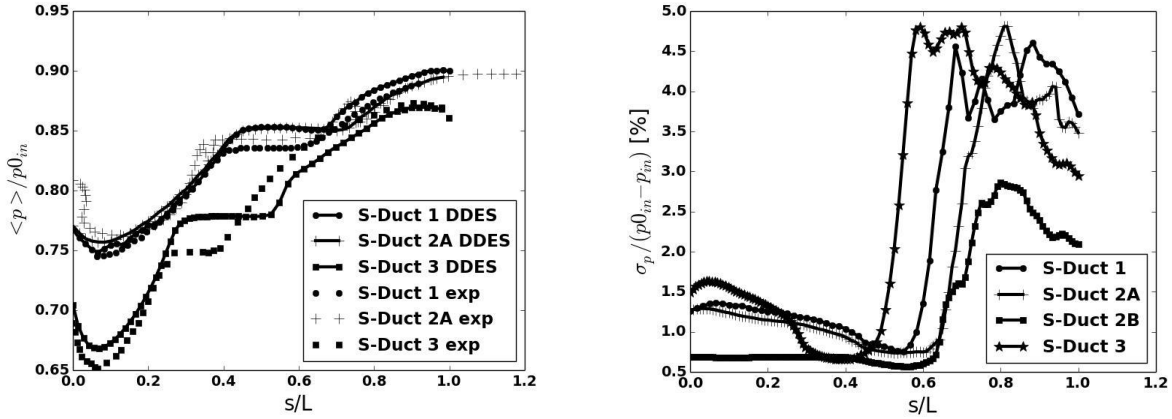

Figure 3: Static pressure distribution on the S-Duct lower wall along the centreline: time-averaged (left), standard deviation (right). Time-averaged values are compared with experimental data from Wellborn et al [1], Delot et al [4] and Garnier et al [5] for S-Duct 1, S-Duct 2A and S-Duct 3 respectively.

4.2. Total pressure and swirl distribution on the AIP

For the 4 test cases considered (**Table 3**), the AIP distribution of the time-averaged pressure recovery (PR) from the 4 DDES calculations is shown in the left hand column of Figure 4 and for these unsteady simulations the right column shows the associated standard deviation of PR. A comparison of the S-Duct 1 pressure recovery distribution with experimental measurements in Wellborn et al [1] revealed a better qualitative agreement of the DDES results in comparison with the RANS simulation distribution in Figure 1. The standard deviation distribution σ_{PR} of S-Duct 1 and 2A with Ma=0.4 is in good qualitative agreement with the measurements reported by Delot et al [4]. For example, the peak value of σ_{PR} of about 3.5% is observed at the external edges of the twin vortices both in the numerical and experimental results.

For the configurations S-Duct 2A and 2B with offset H_o/L=0.268, the relative distribution of time-averaged Pressure Recovery <PR> is qualitatively similar for these cases with higher absolute values of PR at the lower Mach number of 0.18 (Duct 2B, Figure 4). Also the qualitative distribution of the pressure fluctuations σ_{PR} does not change remarkably with Mach number variation, although with a peak value of σ_{PR} of 1% for the low Ma case S-Duct 2B against 3.5% for high Ma (Duct 2A, Figure 4).

The effect of Reynolds number on the pressure recovery characteristics is assessed by comparing the results from Duct 1 and Duct 2A. These have the same non-dimensional geometry and AIP Mach number, but the inlet Re_{Din} for Duct 2A is 1.7×10^6, while it is 2.6×10^6 for Duct 1. The time-averaged pressure recovery distributions of these two cases in Figure 4 are similar, with a slightly lower PR on the lower part of the plane for the low Reynolds case, while its high total pressure zone (PR>0.99) is slightly bigger. No remarkable differences are observed in the σ_{PR} distribution of S-Duct 1 and 2A (Figure 4).

Major differences in the distribution of both the time-averaged pressure recovery <PR> as well as the pressure unsteadiness σ_{PR} are observed for the different geometric configurations where the non-dimensional offset, Ho/L is increased from 0.268 for S-Duct 2A to 0.493 for S-Duct 3. With the higher offset (Ho/L=0.493), the flow separation has a greater impact at the AIP and the low pressure region occupies a much great region of the AIP (Figure 4). For Duct 3 with the increased offset, the zone with the highest fluctuation is now concentrated on the central part of the plane with a higher peak value (σ_{PR} =4.5%) in comparison with the lower offset configuration (S-Duct 2A) where the σ_{PR} was approximately 3.6% and the fluctuations are mainly concentrated on the lower part of the plane (Figure 4)

Figure 5 illustrates the time-averaged and standard deviation distribution of the swirl angle α for the 4 DES simulations. For the S-Duct 1 case, in contrast with the RANS with k-w SST simulation (Figure 2, right), the effect of the twin vortices is concentrated in two smaller regions, in better agreement with Wellborn et al measurements [1]. For the DDES calculations, a comparison between S-Duct 1 and 2A cases with an AIP Mach number of 0.36 reveals a higher swirl angle underneath the twin vortices for the S-Duct 2A case with the smaller diameter and lower Reynolds number. In this case the local peak of time-averaged swirl angle, <α>, is approximately 12 degrees where for the S-Duct 1

configuration the maximum time-averaged α was approximately 7 degrees. A displacement of the radial position of the vortices towards the AIP center as also observed from S-Duct 1 (Re_{Din} =2.6 x 10^6) to S-Duct 2A (Re_{Din} =1.7 x 10^6), with a distance from the center of 60% of the AIP radius for the S-Duct 2A case, against the 70% of the S-Duct 1 case. This can be explained because of the lower curvature radius and diameter of the S-duct 2 which produces a higher adverse pressure gradient and therefore has a stronger secondary flow. In addition, for S-Duct 2A with the lower Reynolds number (Re_{Din} =1.7 x 10^6) relative to the S-Duct 1 configurations (Re_{Din} =2.6 x 10^6) and consequently the viscous origin of the secondary flow and concomitant swirl distortion has a stronger effect on the flow field.

In comparison with the impact on the total pressure distribution, a less remarkable effect of the AIP Mach number on the time-averaged swirl distributions <α> is observed for the S-Duct 2 configuration between Ma=0.4 (Duct 2A) and Ma=0.2 (Duct 2B). The <α> distributions of the S-Duct 2A and 2B cases in Figure 5 appear qualitatively similar with a peak value less than 20% higher for the low Mach case (B). A displacement of the centre of the vortices towards the bottom wall is verified with the decrease of Mach number, where the distance from the plane center increases from the 60% of the radius to the 70%. Modest differences are also observed in the qualitative swirl fluctuation distribution σ_α, with a peak value 15% higher when the AIP Ma is increased from 0.18 (S-Duct 2B) to 0.36 (S-Duct 2A, Figure 5).

As expected, major effects are observed due to the effect of the non-dimensional S-duct offset (Ho/L). Indeed, when Ho/L is increased from 0.268 (S-Duct 2A) to 0.493 (S-Duct 3) the time-averaged location of the twin vortices moved toward the central part of the AIP and their effect is extended to a upper region of the plane. Moreover, the peak value of < α > increases from 12 to 20 deg. The peak value of the swirl fluctuations σ_α is similar for both of the cases, but for S-Duct 3 (Ho/L=0.493) the extent of the region with high fluctuations extends to about 70% of the AIP which it is approximately an extent of 50% for the S-Duct 2A configuration with a lower offset (Ho/L=0.268).

4.3.Flow distortion assessment

The statistics of the temporal distribution of the flow distortion parameters and pressure recovery are summarized in **Table 3**. For comparison, data from RANS are included for the cases S-Duct 1 and 2A. For the unsteady simulations, the average value of the distortion parameter are reported together with the standard deviation σ and peak value "max" and the minimum value is reported for the pressure recovery PR. Some tests suggest a relation between peak distortion and the onset of surge, as reported in the planar wave investigations reported by the SAE [18].

A comparison between RANS and DDES time-averaged distortion descriptors in **Table 3** shows noticeable differences. Whilst time averaged pressure recovery <PR> varies by less than 2% from the steady to transient simulations, both for S-Duct 1 and 2A, DC(60) reduces by about 30% for S-Duct 1 and by 20% for S-Duct 2. More remarkable is the variation of the swirl coefficient SC(60), where the value from DDES is more than twice that calculated by RANS. Large oscillations of the swirl angle are taken into account with unsteady simulations. An increase of up to 30% is observed for CDI. For the radial distortion, a large variation from RANS to DDES is observed only for the lower diameter case S-Duct 2A.

As expected, the total pressure flow distortion is sensitive to the operating Mach number and when the AIP Ma is reduced from 0.36 (Duct 2A) to 0.18 (Duct 2B) there is a reduction of about 3.4% in the time averaged pressure recovery, <PR> (**Table 3**). There is also a substantial reduction in the RDI and CDI values and overall the time-averaged CDI and RDI reduce by a factor of 3.9 and 3.5, respectively, when the AIP Mach number is reduced from 0.36 to 0.18 (**Table 3**). Although there are still some occasional brief increases in RDI, the average RDI is also now reduced in comparison with the configuration with a greater Ma of 0.36.

The maps in Figure 6 show the distribution of the simultaneous radial (RDI) and circumferential (CDI) total pressure distortion for the 4 configurations (Table 2) calculated using the DDES method. In the unsteady RDI-CDI map for the S-Duct 1 configuration there is a relatively equal distribution of points in a range of variation of CDI of about 0.08) and a variation of RDI of about 0.03. This variation can be considered in terms of the vertical and lateral oscillations of the separation region. However, a smaller amount of data points is also scattered outside this area. In particular in the top-right part of the map it can be observed that there are exceptional peak values of radial distortion related to high values of CDI. This can be explained as instability in the separation zone, with propagation at irregular intervals of vortical structures to the higher part of the AIP normally not crossed by the primary separation.

In comparison with the datum S-Duct 1 configuration, for the same geometric shape investigated by Delot et al [4] (S-Duct 2A), but at a lower inlet diameter and therefore the Reynolds number (Re_{Din}=1.7 x 10^6), a similar map is observed. With this reduction in Reynolds number, there is a slight increase in the average CDI from 0.079 to 0.091 although the average RDI is the same at about 0.033. There is a slight reduction in CDI fluctuations σ_{CDI} from 0.018 to 0.014 and a

slight increase in σ_{RDI} from 0.007 to 0.008. In addition, there is a broadly similar characteristic of large occasional increases in RDI without any notable associated change in CDI.

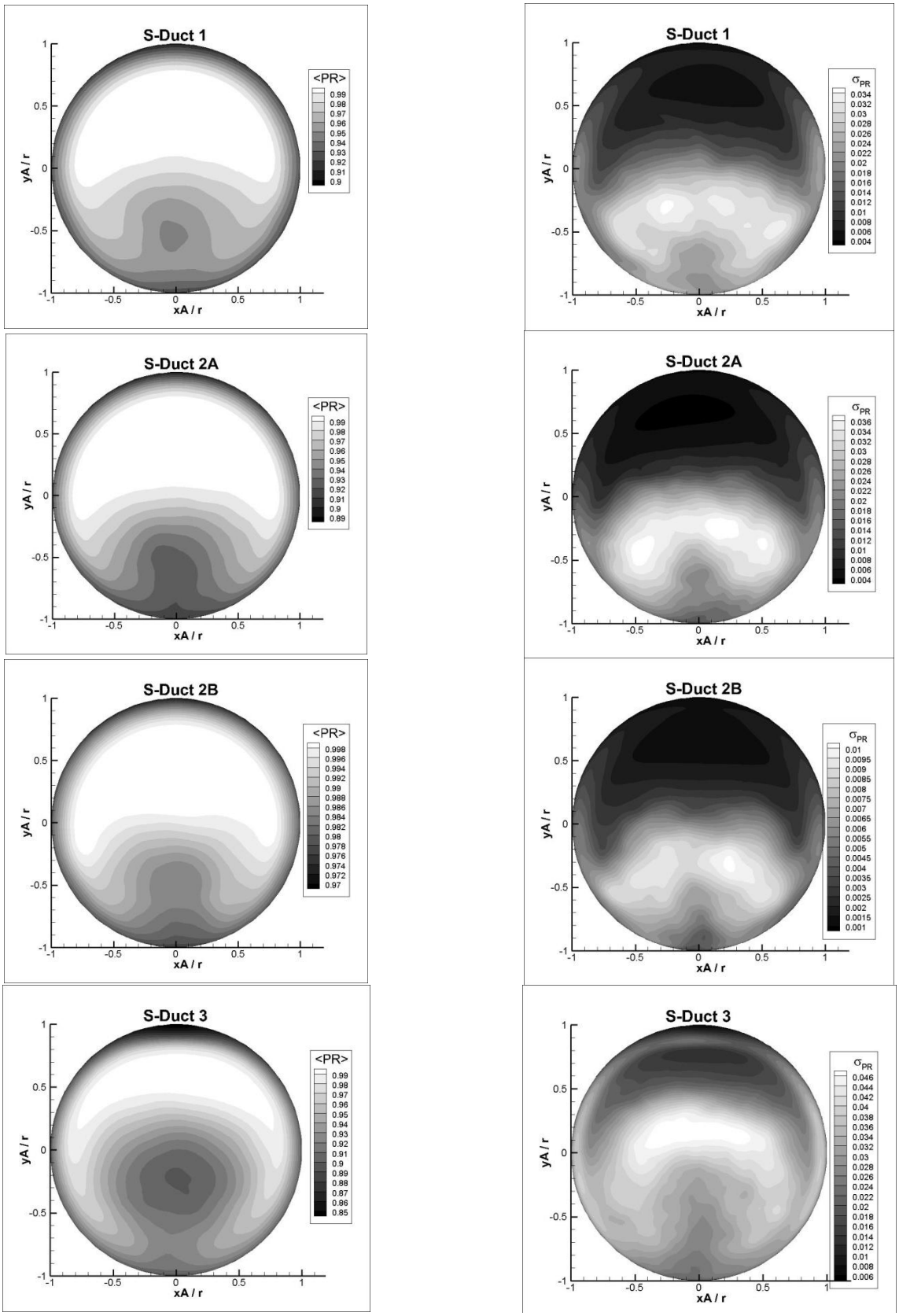

Figure 4: Pressure recovery time averaged and standard deviation at the AIP from DDES.

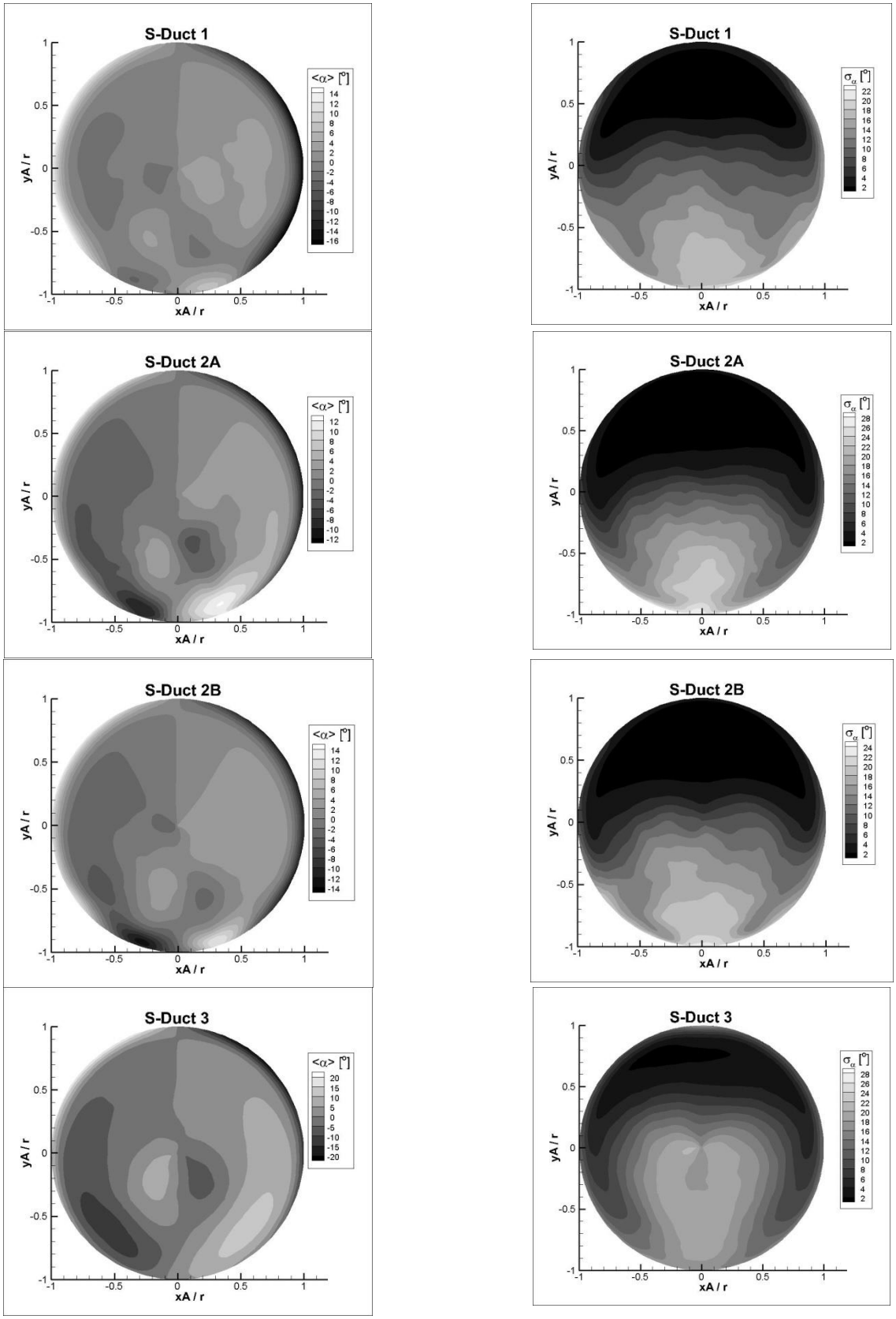

Figure 5: Swirl angle distributions at the AIP from DDES. Time-averaged (left) and standard deviation (right)

For the S-Duct 3 configuration where the S-duct offset H0/L is increased from 0.268 to 0.493, there is a notable increase in both the time averaged RDI and CDI distortion levels as well as an increase in the extreme values. Time average CDI and RDI increase from 0.09 to 0.10 and from 0.033 to 0.050, respectively. With this more aggressive duct, there is a more notable scatter in the RDI distribution in particular where the standard deviation of RDI has almost tripled from approximately 0.008 to 0.024.

Figure 7 highlights the level of agreement between CFD and experiment trend for the variations of the main time averaged performance parameters for two different Mach numbers at the AIP and two different offset ratios (H/L=0.268 and 0.493). Although there are differences in the absolute values calculated by the CFD relative to the measurements, there is some agreement in the trends and relative variations.

Case	<PR>	DC(60)	SC(60)	CDI	RDI
S-Duct 1 RANS	0.970	0.549	0.081	0.065	0.030
S-Duct 1 DDES	Avg: 0.972 Min: 0.968 Std: 0.002	Avg: 0.370 Max: 0.822 Std: 0.154	Avg: 0.204 Max: 0.390 Std: 0.058	Avg: 0.079 Max: 0.136 Std: 0.018	Avg: 0.033 Max: 0.071 Std: 0.007
S-Duct 2A RANS	0.968	0.603	0.094	0.070	0.022
S-Duct 2A DDES	Avg: 0.968 Min: 0.963 Std: 0.002	Avg: 0.505 Max: 0.793 Std: 0.114	Avg: 0.222 Max: 0.377 Std: 0.044	Avg: 0.091 Max: 0.142 Std: 0.014	Avg: 0.033 Max: 0.099 Std: 0.008
S-Duct 2B DDES	Avg: 0.992 Min: 0.991 Std: 0.001	Avg: 0.427 Max: 0.796 std: 0.141	Avg: 0.213 Max: 0.387 std: 0.052	Avg: 0.023 Max: 0.040 Std: 0.005	Avg: 0.009 Max: 0.019 Std: 0.002
S-Duct 3 DDES	Avg: 0.947 Min: 0.938 Std: 0.002	Avg: 0.334 Max: 0.628 Std: 0.088	Avg: 0.268 Max: 0.420 Std: 0.044	Avg: 0.103 Max: 0.206 Std: 0.016	Avg: 0.050 Max: 0.153 Std: 0.024

Table 3: Summary of the performance parameter results. For DDES time-averaged value (avg), standard deviation (std) and peak value (max) are outlined.

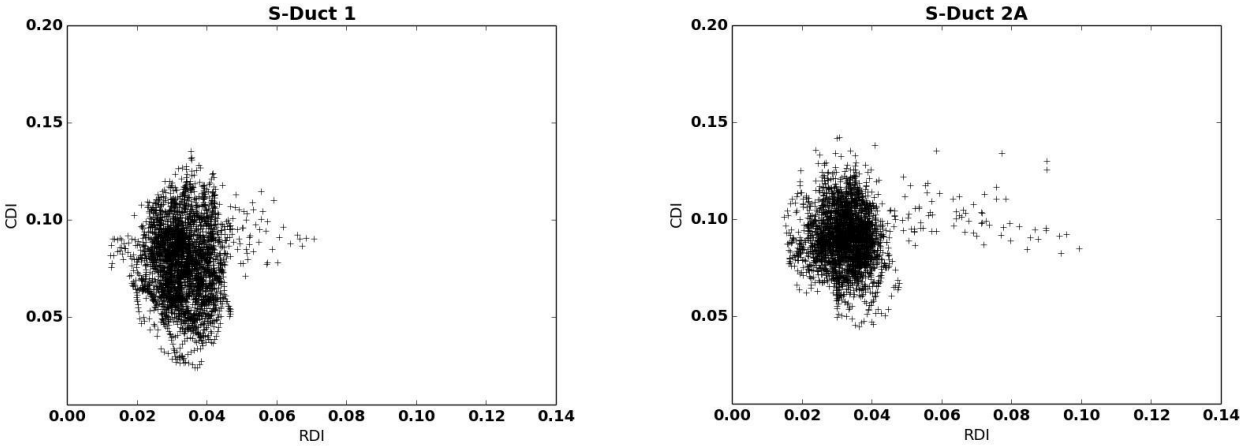

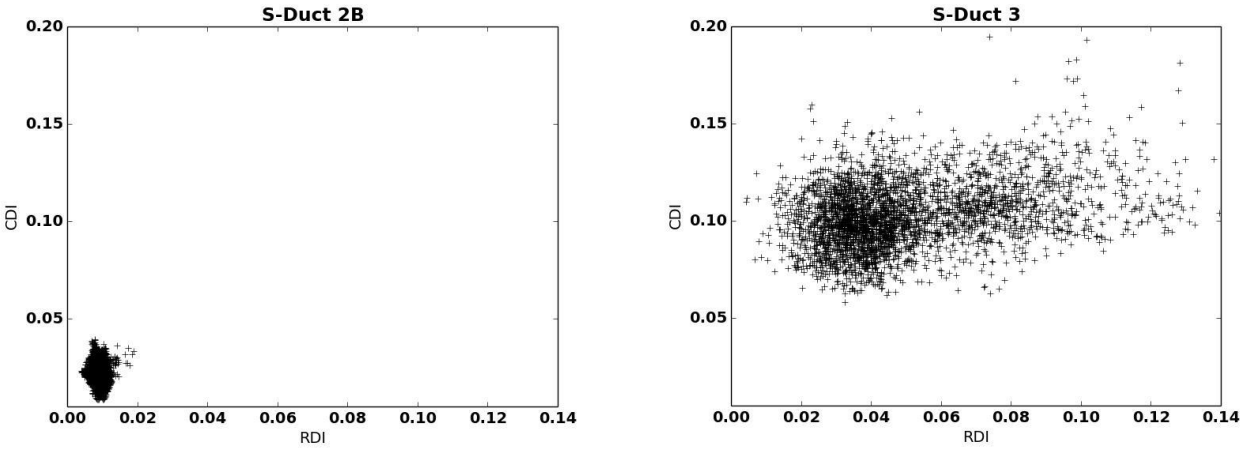

Figure 6: RDI/CDI maps

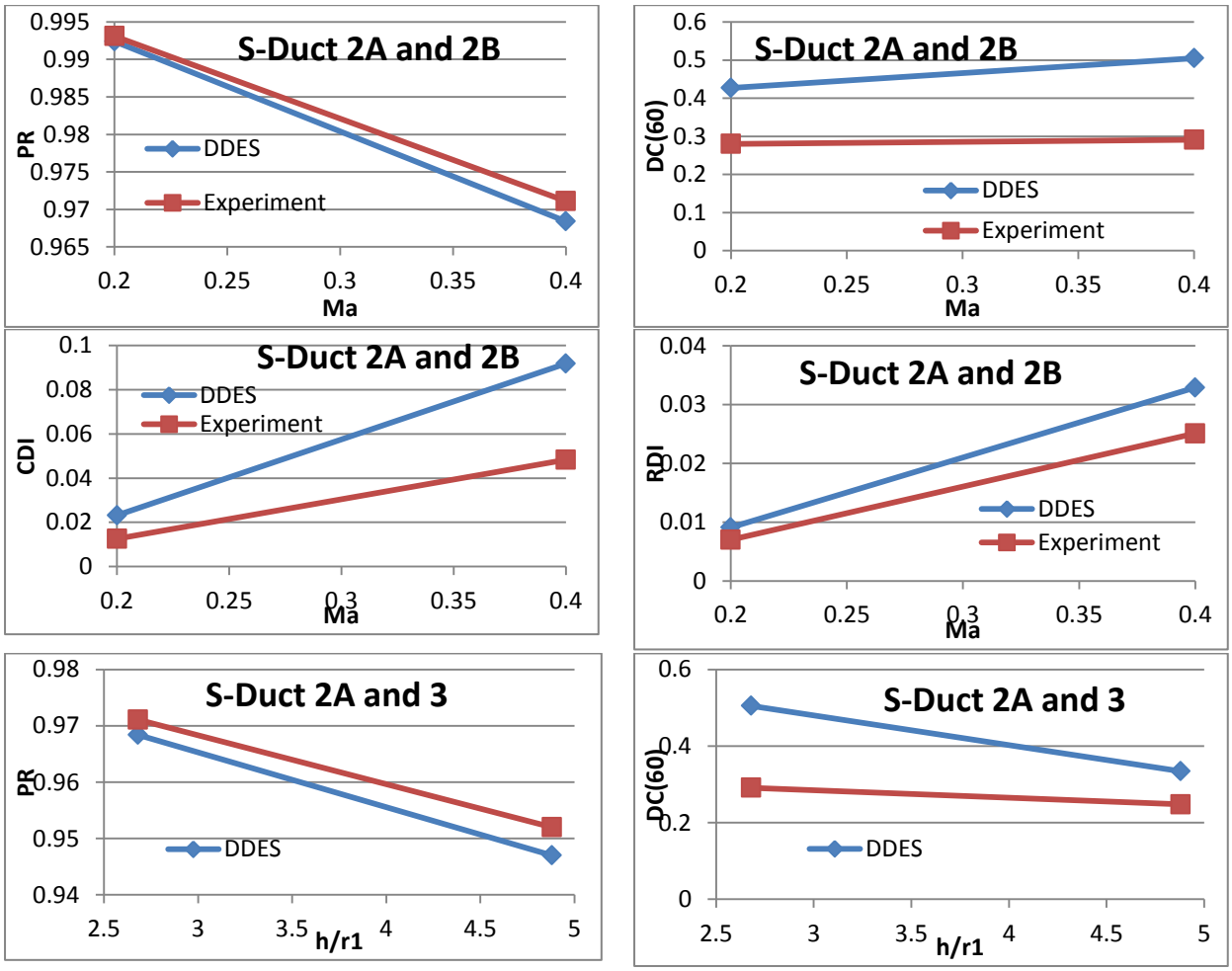

Figure 7: Time averaged performance variations and comparison with experimental data reported in Delot et al [6] and Garnier et al [5].

4.4.Flowfield spectral analysis at the AIP

According to the SAE report on planar waves [18], compressor sensitivity on flow distortion depends also on the frequency of the unsteadiness. For the current DDES calculations, the unsteady flow field at the AIP has been analysed and the distribution of the total pressure fluctuations σ_{PR} divided in frequency bands of 100 Hz presented for S-Duct 1, S-Duct 2 and S-Duct 3 (Figure 8, Figure 9 and Figure 10, respectively). As a consequence of the unsteady behaviour of the flow, some asymmetry is still observed and a longer simulation time is necessary for a fully symmetric distribution to be established. However, the main features can be clearly identified.

Figure 8 shows the spectral distribution of σ_{PR} for S-Duct 2A case with offset H0/L=0.268 and AIP Ma=0.36. The highest fluctuation energy is concentrated in the [200-300] HZ band, where is represented the main feature of the complete σ_{p0} distribution for S-Duct 2A in Figure 4, i.e. an high fluctuation zone on the external edge of the twin vortexes, in the edge between the low and high total pressure zones illustrated in the time averaged distribution <p0> in Figure 4. The peak value in this interval is also close to the peak of σ_{PR} in the complete distribution in Figure 4 (2.6% against 3.6%). High energy content is also observed in the band [500-600] Hz, where a peak higher than 2% is located on the central part at a distance of 25% of the radius from the center, at the edge between the low and high p0 areas of the time-averaged field, located above the main vortex pairs (Figure 8). The superimposition of bands [200-300] and [500-600] reproduces most of the features observed in the σ_{PR} distribution in Figure 4. Slightly lower intensity is observed at lower frequencies ([0-100] and [100-200] Hz in Figure 8). In the interval [200-600] Hz, fluctuations extend also to the upper part of the plane, in particular close to the wall. The intensity and extent of the unsteady regions progressively reduces for frequencies higher the 600 Hz (Figure 8, lower). Spectral distribution of the circumferential distortion CDI is outlined in Figure 11 left, where the two main components can be noticed at about 300 and 500 Hz.

Spectral distribution of σ_{PR} for the same geometry but a lower AIP Mach number of 0.18 is shown in Figure 9 (S-Duct 2B). In comparison with the higher Ma case S-Duct 2A (Figure 8) fluctuations are more concentrated at the lower frequencies. The features observed at [200-300] and [500-600] Hz in Figure 8 for S-Duct 2A, for the low Mach case (Figure 9) are observed at [100-200] and [200-300] Hz respectively. This suggests a shift in frequency with a decrease of Mach number without remarkable variation of the major flow structure. Oscillation peaks was observed at about 115 Hz and 230 Hz for the intervals [100-200] Hz and [200-300] Hz respectively, which are close to the values of 110 and 220 Hz measured in Delot et al [4], with similar geometry and flow conditions. The spectral distribution of CDI in Figure 11, center, shows a peak at 230 Hz. The frequency band distribution of σ_{PR} is Figure 9 is in good agreement with the experimental distribution reported by Delot et al [4]. For the low Mach case (S-Duct 2B, Ma=0.18), the cross-correlation of the total pressure temporal distribution was calculated between two opposite points with respect to the y-axis, in the zone of maximum fluctuation. Figure 12 shows the graph of coherence and phase, with two significant level of coherence at 115 and 230 Hz. The phase graph Figure 12 shown that the two oscillations are in phase at 230 Hz and out of phase at 115 Hz. This suggests an association of the first with vertical oscillation of the separation zone, while the 115 Hz component is related to lateral oscillation of the vortexes.

The spectral distribution of σ_{PR} and CDI for the high offset S-Duct (S-Duct 3, Ho/L=0.493) are outlined in Figure 10 and Figure 11 right. The comparison with the CDI power spectrum for the low offset case S-Duct 2A (Figure 11, right) with Ho/L=0.268 shows a shift in frequency, with peak values now observed around 600 and 800 Hz. It can be noticed in Figure 10 that the fluctuations extend throughout the AIP for all the bands illustrated. The highest energy content is in the band [400-500] Hz, with two opposite high fluctuation areas translated upwards in comparison with the low Mach case (Figure 8) in the interval [200-300] Hz

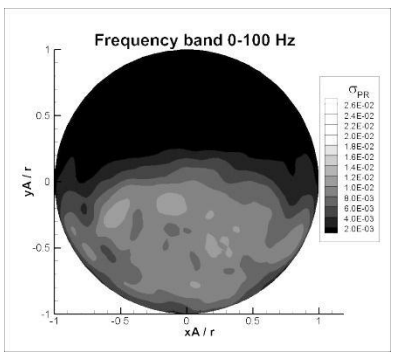

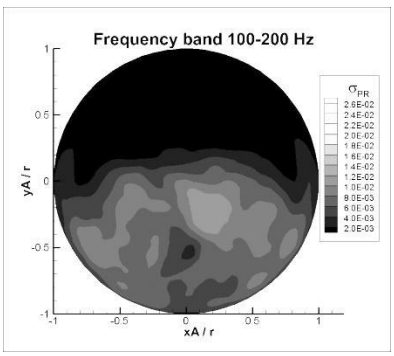

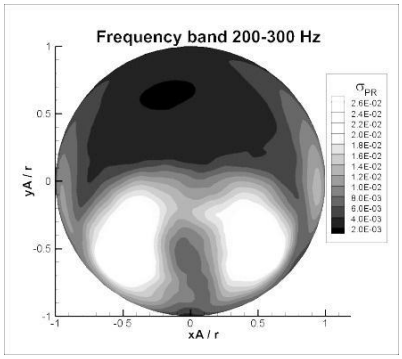

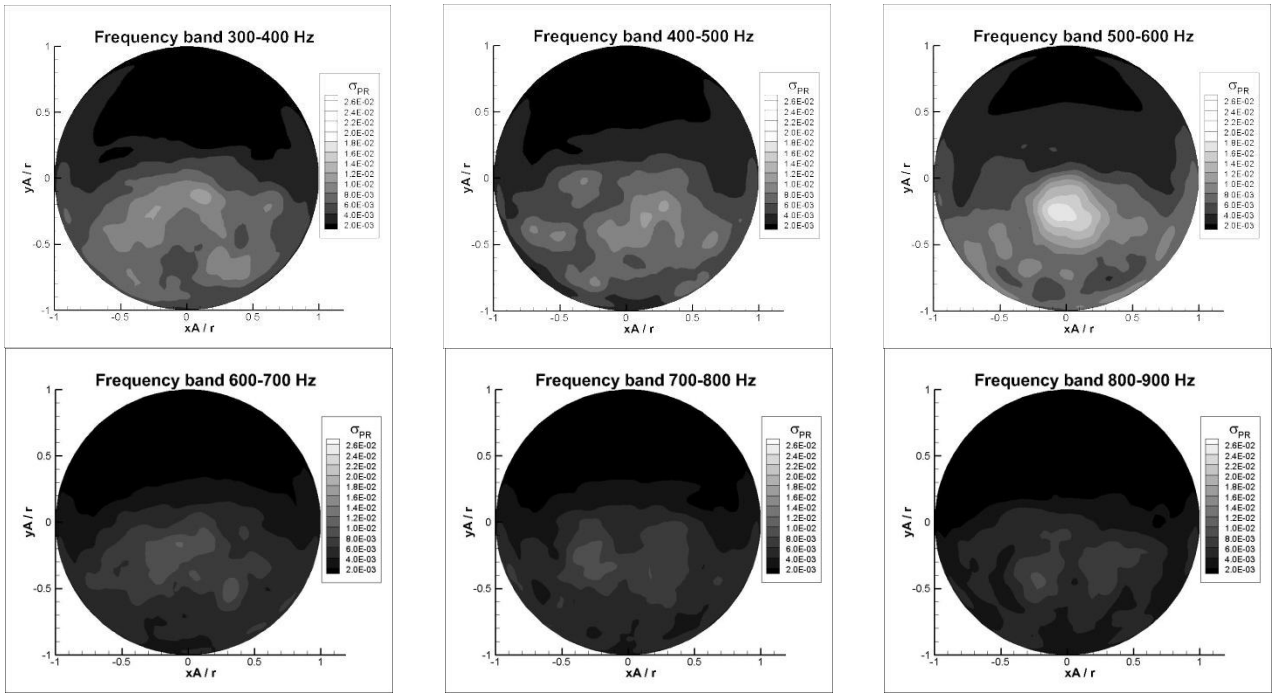

Figure 8: AIP spectral distribution of total pressure fluctuations for the case S-duct 2A

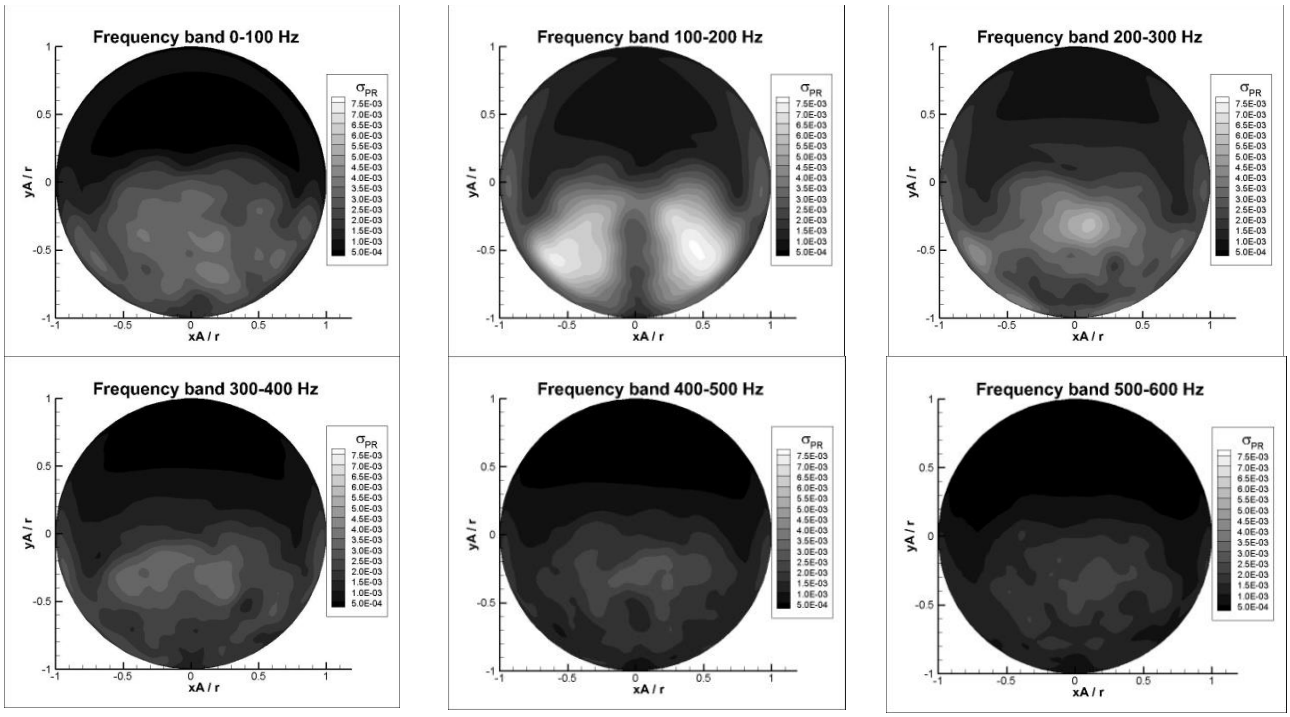

Figure 9: AIP spectral distribution of total pressure fluctuations for the case S-duct 2B

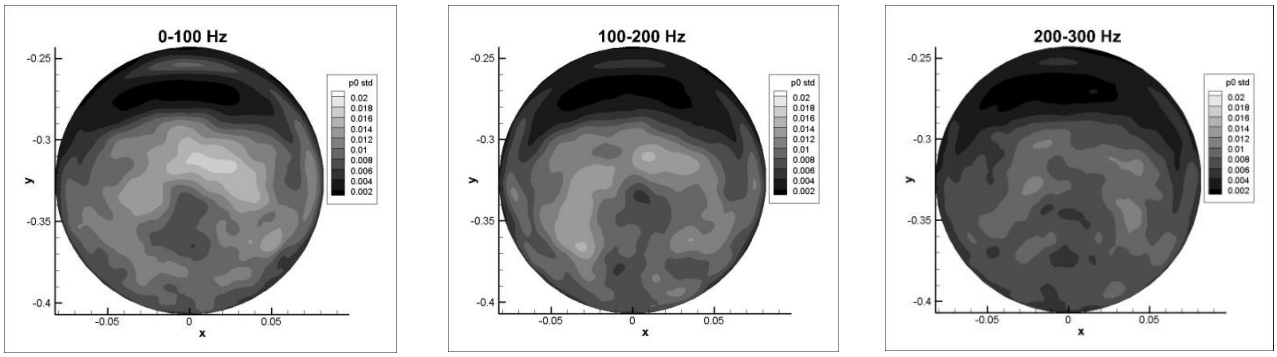

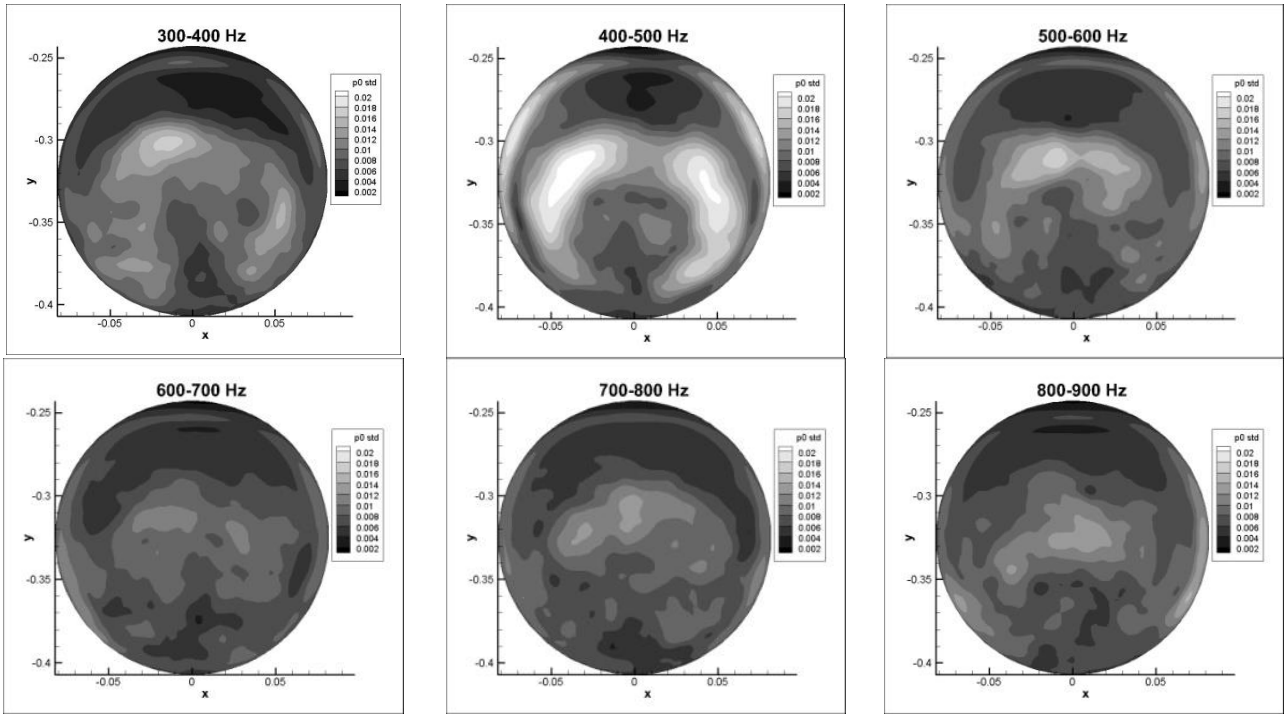

Figure 10: AIP spectral distribution of total pressure fluctuations for the case S-duct 2A

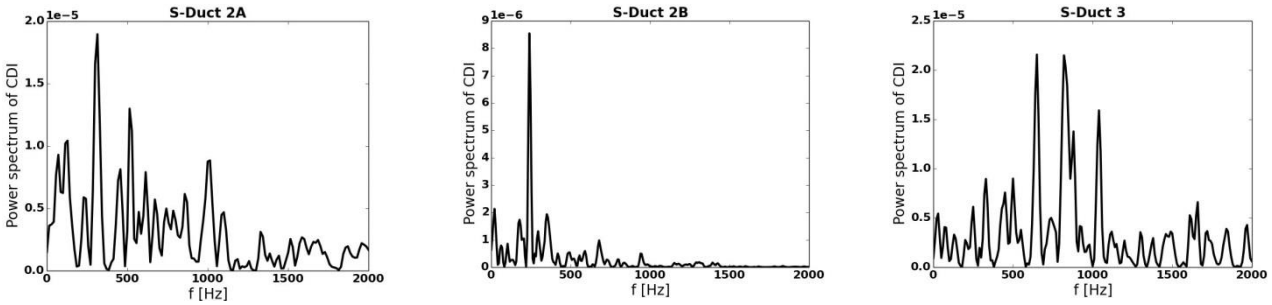

Figure 11: Power Spectrum of circumferential distortion CDI for the S-Duct 2A (left), 2B (center) and 3 (right).

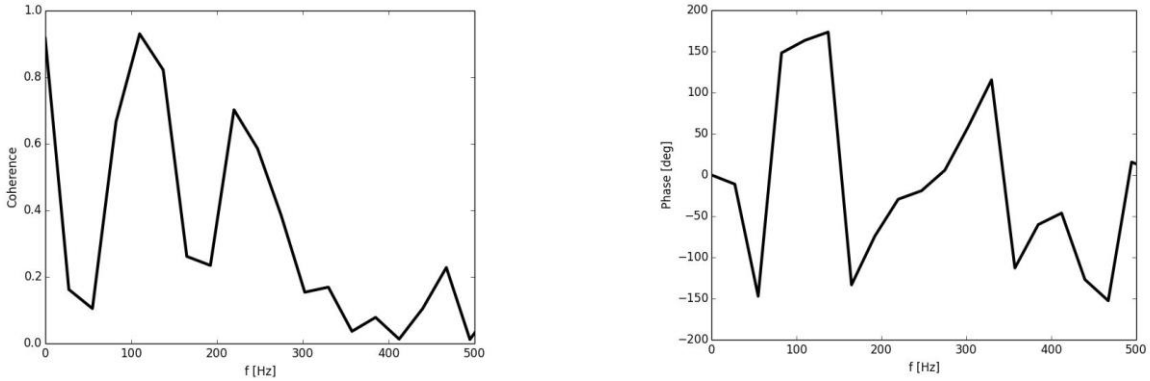

Figure 12: coherence and phase distribution between two opposite points on the AIP for the case S-Duct 2B.

4.5. Proper Orthogonal Decomposition (POD) analysis

To develop a better understanding of the unsteady behaviour of the flow and the underlying flow structures, the use of the Proper Orthogonal Decomposition (POD) method was applied to the total pressure distribution. The impact of Mach number and non-dimensional offset Ho/L was investigated. For this aspect, the time-history of the total pressure at the AIP was decomposed using POD to reveal the main flow modes. The modes are sorted by the energetic content of their signal in descending order.

Figure 13 and Figure 14 outline the distribution for the highest energy modes for the cases S-Duct 2A (Ho/L=0.268 and AIP Ma=0.36) and S-Duct 2B with the same geometry and Ma=0.18. The distribution of the variance for the POD coefficients "a" (as a percentage of the total variance content) for the first 10 modes is illustrated (top-left), followed by the AIP distribution of the modes 1 to 5. For all the cases, mode 0, not shown here, has an identical distribution to the time-averaged total pressure distribution is illustrated in Figure 4. For the high Mach case S-Duct 2A (Figure 13), mode 1 has the highest variance of the coefficient "a" temporal distribution. It is characterized by an anti-symmetric distribution and is representative of an out of phase oscillation between opposite points at the lower part of the AIP, with a shape that reproduces the main features of the σ_{PR} distribution of Figure 8. Mode 2, which has half magnitude of the variance of mode 2, has a symmetric distribution with respect to the y axis and appears similar to σ_{PR} of Figure 8 for the interval [500-600] Hz. Mode 3 and 4 also have a symmetric distribution and produce a vertical oscillation of the total pressure field. Mode 5 mostly represents an out of phase oscillation of opposite points with respect to y-axis at the lower wall. Figure 14 shows a distribution of the POD coefficients and modes for a low Mach number (S-Duct 2A) with the same duct geometry (Figure 13). Mode 1 and 2 appear very similar for both of the cases. Some difference is seen for modes 3,4 and 5.

A strong impact of the offset is observed in the comparison between Figure 13 for Duct 2A (Ho/L=0.268), and Figure 15 for S-Duct 2B (Ho/L=0.493). For the high offset case, mode 1 and 2 are occupied by two orthogonal distributions with similar variance, which represents two inclined, out of phase oscillations. Mode 3 mainly represents an oscillation with vertical total pressure gradient while mode 4 represents a horizontal-gradient oscillation with point opposite with respect to y-axis out of phase, similar to what observed in mode 1 for the low offset case S-Duct 2A. Mode 5 highlights oscillations at the central part of the plane.

In order to assess the relation between the POD mode distribution and total pressure distortion, the value of RDI and CDI for the signal reconstructed with different number of modes is plotted in Figure 16, normalized with the value of the full signal. It can be noticed that CDI requires a high number of modes to be accurately reproduced, in strong contrast with RDI. This suggests a strong dependence of the circumferential distortion on both the major and the finer structures of the distorted flow field.

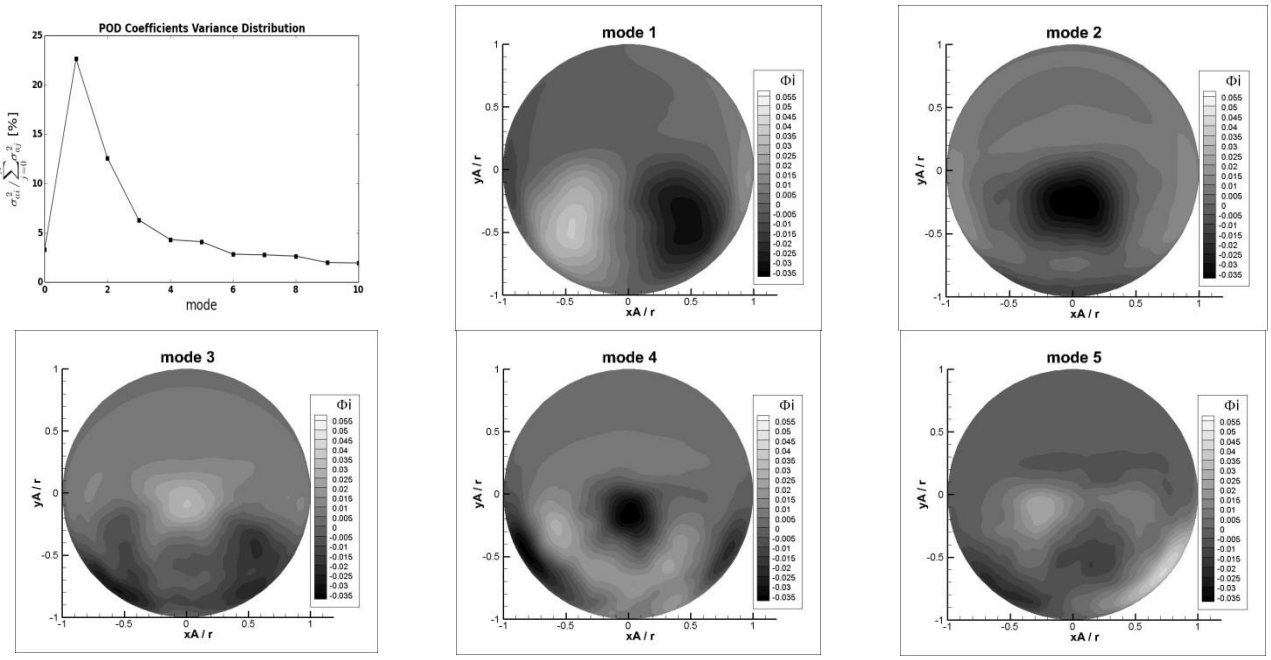

Figure 13: POD coefficients variance for mode 1 to 10 (top-left) and AIP distribution of mode 1 to 5 for the case S-Duct 2A.

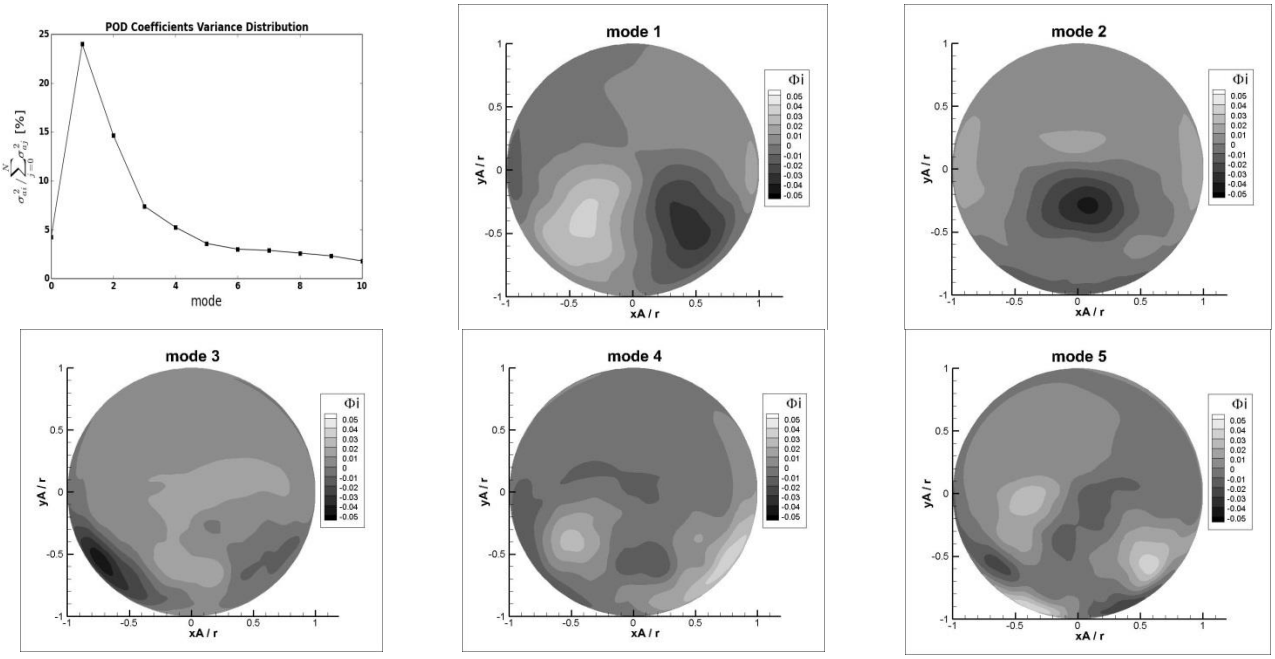

Figure 14 POD coefficients variance for mode 1 to 10 (top-left) and AIP distribution of mode 1 to 5 for the case S-Duct 2B.

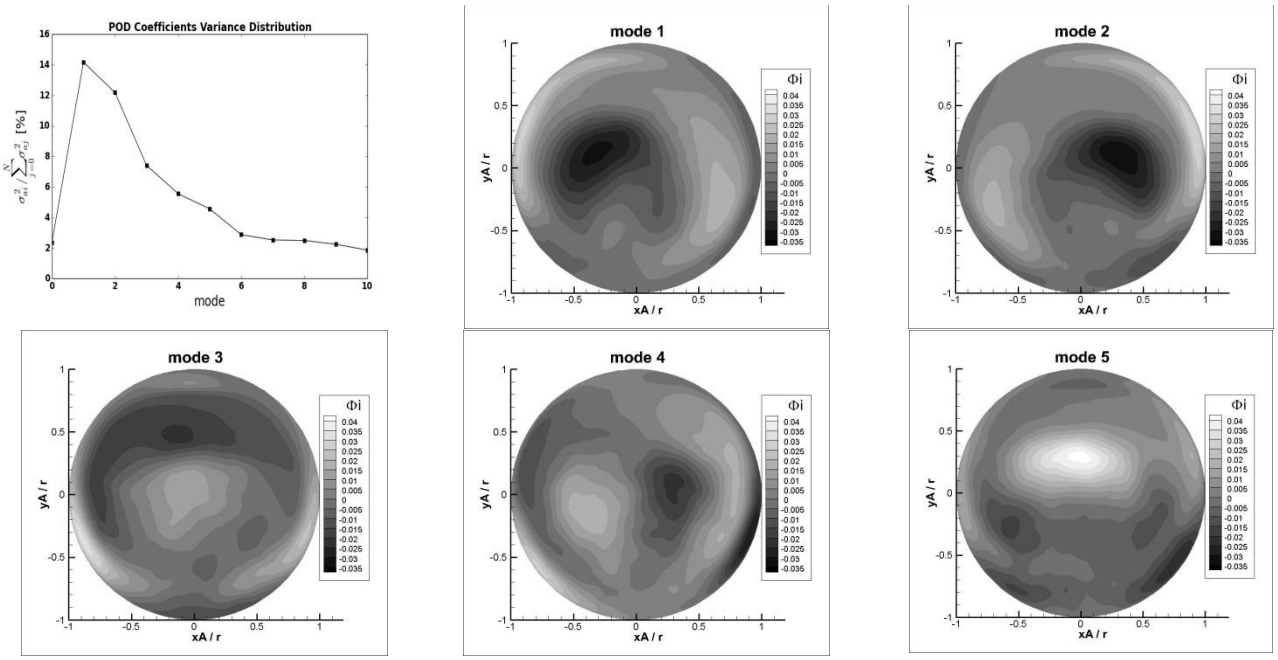

Figure 15 POD coefficients variance for mode 1 to 10 (top-left) and AIP distribution of mode 1 to 5 for the case S-Duct 3.

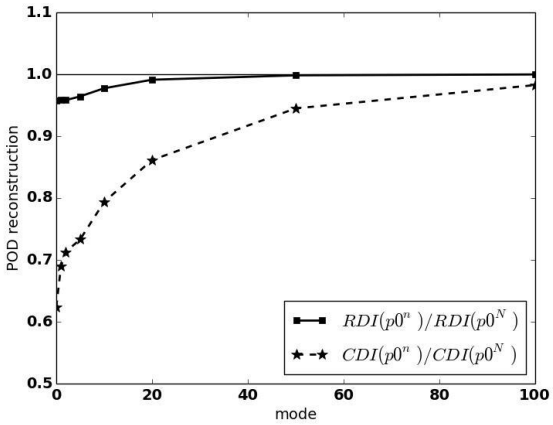

Figure 16: RDI and CDI of the POD-reconstructed signal for different number of modes, normalized with the values of the full signal.

5. Conclusions

A parametric study of the S-Duct offset, AIP Mach number and duct Reynolds number on the dynamic flow distortion was performed. Generally, a good qualitative agreement with experimental data available in literature was observed. In particular the simulations correctly predicted the trend of variation of pressure recovery and flow distortion parameter against the main duct geometric and flow parameters even if the absolute values are not still accurately predictable by CFD. Thus, although the accuracy in intake flow distortion calculation has some limitations for design applications, the capability to predict changes in performance for different configurations suggest a combined application of RANS and DDES for intake shape optimization for reduction of static and dynamic distortion.

The proper orthogonal decomposition of the AIP time resolved total pressure distribution identified the main deterministic structures of the underlying flow fields. It was observed a stronger impact of the S-Duct offset on the main flow structures shape in comparison with Mach number. The flow distortion analysis of the signal reconstruction showed the dependency of the flow distortion not only on major structures of the flow, but also the finer flow field characteristics. This should be considered in future intake-compressor compatibility assessments.

References

[1] S. R. Wellborn, T. H. Okiishi and B. A. Reichert, "A study of the Compressible Flow Through a Diffusing S-Duct," NASA Technical Memorandum 106411, USA, 1993.

[2] S-16 Turbine Engine Inlet Flow Distortion Committee, A methodology for Assessing Inlet Swirl Distortion, USA: No. AIR5686, Society of Automotive Engineers, 2007.

[3] S-16 Turbine Engine Inlet Flow Distortion Committee, “Inlet Total-Pressure-Distortion Considerations for Gas-Turbine Engines,” No. AIR1419, Society of Automotive Engineers, USA, 1999.

[4] A.-L. Delot, E. Garnier and D. Pagan, “Flow Control in a High-Offset Subsonic Air Intake,” in *47th AIAA/ASME/SAE/ASEE Joint Propulsion Conference & Exhibit, AIAA 2011-5569*, San Diego, California, USA, 2011.

[5] E. Garnier, M. Leplat, J. C. Monnier and J. Delva, “Flow control by pulsed jet in a highly bended S-duct,” AIAA 2012-3250, 6th AIAA Flow Control Conference, New Orleans, Louisiana, USA, 2012.

[6] A.-L. Delot and R. K. Schamhorst, “A Comparison of Several CFD Codes with Experimental Data in a Diffusing S-Duct,” AIAA 2013-3796, San Jose, USA, 2013.

[7] T. M. Berends, A.-L. Delot, M. Chevalier, J. Van Muijden, R. A. Waaijer and P. Tattersall, “GARTEUR AD/AG-43: Application of CFD to High Offset Intake Diffusers,” Final Report, 2002.

[8] A.-L. Delot, T. M. Berens, M. Tormalm, M. Säterskog and N. Ceresola, “DES Computations for a Subsonic UAS Configuration with a Highly Integrated S-Shaped Inlet Duct,” in *AIAA SciTech, 52nd Aerospace Sciences Meeting, AIAA 2014-0723*, Maryland, USA, 2014.

[9] D. C. Wilcox, Turbulence modelling for CFD, DCW Industries, 2006.

[10] F. R. Menter, M. Kuntz and R. Langtry, “Ten Years of Industrial Experience with the SST Turbulence Model,” *Turbulence, Heat and Mass Transfer,* 2003.

[11] P. S. Spalart, “Detached-Eddy Simulation,” *The Annual Review of Fluid Mechanics,* vol. 41, pp. 181-202, 2008.

[12] L. Penin, Computation Analysis of Swirl Distortion in a Diffusing S-Duct, MSc Thesis, Cranfield University, 2003.

[13] P. J. Roache, Verification and Validation in Computational Science and Engineering, Albuquerque, USA: Hermosa Publishers, 1998.

[14] B. H. Anderson, H. D. Baust and J. Agrell, Management of Total Pressure Recovery, Distortion and High Cycle Fatigue in Compact Air Vehicule Inlets, NASA/TM 2002-212000, 2002.

[15] Y. Coling, B. Aupoix, J. F. Boussuge and F. Chanez, Numerical Simulation of the Distortion Generated by Crosswind Inlet Flows, ISABE-2007-1210, 2007.

[16] N. C. Bissinger and T. Breuer, “Basic Principles - Gas Turbine Comptatibility - Intake Aerodynamics Aspects,” in *Encyclopedia of Aerospace Engineering, Volume 8, Chapter EAE487*, Richard Blockley and Wei Shyy, 2010.

[17] E. L. Goldsmith and J. Seddon, Intake Aerodynamics, second edition, vol. second edition, Blackwell Scientific Publications, 1999.

[18] Society of Automotive Engineering, “A Current Assessment of Planar Waves,” 1995.

[19] A. Silva Lopes, U. Piomelli and J. Palma, “Large eddy simulation of the flow in an S-duct,” in *41st Aerospace Sciences Meeting and Exhibit 6-9 January 2003*, Reno, Nevada, 2003.

[20] P. S. Bernard and J. M. Wallace, Turbulent Flow. Analysis, Measurement, and Prediction, Hoboken, New Jersey: John Wiley & Sons, Inc, 2002.

[21] P. G. Tucker, Unsteady Computational Fluid Dynamics in Aeronautics, Springer, 2013.

[22] P. Tucker, “Computation of Unsteady Turbomachinary Flows- Part: 2- LES and hybrids,” *Progress in Aerospace Sciences,* vol. 47, pp. 546-569, 2011.